A Room-Temperature Spin-Valve with van der Waals Ferromagnet Fe<inf>5</inf>GeTe<inf>2</inf>/Graphene Heterostructure

N.B. When citing this work, cite the original published paper.

(article starts on next page)

A Room-Temperature Spin-Valve with van der Waals Ferromagnet Fe$_5$GeTe$_2$/Graphene Heterostructure

Bing Zhao, Roselle Ngaloy, Sukanya Ghosh, Soheil Ershadrad, Rahul Gupta, Khadiza Ali, Anamul Md. Hoque, Bogdan Karpiak, Dmitrii Khokhriakov, Craig Polley, Balasubramanian Thiagarajan, Alexei Kalaboukhov, Peter Svedlindh, Biplab Sanyal,* and Saroj P. Dash*

The discovery of van der Waals (vdW) magnets opened a new paradigm for condensed matter physics and spintronic technologies. However, the operations of active spintronic devices with vdW ferromagnets are limited to cryogenic temperatures, inhibiting their broader practical applications. Here, the robust room-temperature operation of lateral spin-valve devices using the vdW itinerant ferromagnet Fe$_5$GeTe$_2$ in heterostructures with graphene is demonstrated. The room-temperature spintronic properties of Fe$_5$GeTe$_2$ are measured at the interface with graphene with a negative spin polarization. Lateral spin-valve and spin-precession measurements provide unique insights by probing the Fe$_5$GeTe$_2$/graphene interface spintronic properties via spin-dynamics measurements, revealing multidirectional spin polarization. Density functional theory calculations in conjunction with Monte Carlo simulations reveal significantly canted Fe magnetic moments in Fe$_5$GeTe$_2$ along with the presence of negative spin polarization at the Fe$_5$GeTe$_2$/graphene interface. These findings open opportunities for vdW interface design and applications of vdW-magnet-based spintronic devices at ambient temperatures.

1. Introduction

The creation of van der Waals (vdW) heterostructures by combining 2D quantum materials with complementary properties can allow the discovery of basic new physical phenomena and the development of new device concepts.[1] The discovery of new vdW quantum materials and their heterostructures starting from graphene, insulators, semiconductors, superconductors, and topological materials has revolutionized both fundamental and applied research.[2,3] The most recent addition to this vdW family is magnets, which have offered various advantages over conventional magnets and opened new perspectives in vdW heterostructure designs.[4–6] In addition to the atomically thin and flat nature of vdW magnets, flexibility, gate tunability, strong proximity interactions, and twist angle between the layers can offer a unique degree of freedom and an innovative platform for device functionalities.[4,5]

Recently, several vdW magnets have emerged with the discovery of insulating Cr$_2$Ge$_2$Te$_6$,[7] semiconducting (CrI$_3$,[8] CrBr$_3$[9]), and metallic Fe$_x$GeTe$_2$.[10,11] The insulating vdW magnets are useful for spin-filter tunneling[9,12] and proximity-induced magnetism,[13–15] whereas the metallic magnets can be used as electrodes in magnetic tunnel junctions,[16] observation

B. Zhao, R. Ngaloy, K. Ali, A. Md. Hoque, B. Karpiak, D. Khokhriakov,
A. Kalaboukhov, S. P. Dash
Department of Microtechnology and Nanoscience
Chalmers University of Technology
Göteborg SE-41296, Sweden
E-mail: saroj.dash@chalmers.se
S. Ghosh, S. Ershadrad, R. Gupta, B. Sanyal
Department of Physics and Astronomy
Uppsala University
Box 516, Uppsala SE-751 20, Sweden
E-mail: biplab.sanyal@physics.uu.se

R. Gupta, P. Svedlindh
Department of Materials Science and Engineering
Uppsala University
Box 35, Uppsala SE-751 03, Sweden
K. Ali, C. Polley, B. Thiagarajan
MAX IV Laboratory
Lund University
Lund SE-221 00, Sweden
S. P. Dash
Graphene Center
Chalmers University of Technology
Göteborg SE-41296, Sweden

ADVANCED
SCIENCE NEWS

www.advancedsciencenews.com

ADVANCED
MATERIALS

www.advmat.de

of skyrmions[17] and spin-orbit-torque memory devices[18,19] for energy-efficient and ultra-fast spintronic technologies. However, the demonstration of these device operations with vdW magnets is so far limited to cryogenic temperatures. Although room temperature magnetism and proximity effects have been reported using vdW magnets,[20–22] the lack of active spintronic device operation at room temperature significantly limits its practical application potential.[21,23,24] Furthermore, a lateral room temperature spin-valve device with vdW metallic magnets, an essential building block for proposed spin-based memory, logic, and neuromorphic computing architectures[25–28] has not been realized yet.

Here, we demonstrate robust room-temperature lateral spin-valve device operations using Fe_5GeTe_2/graphene heterostructures. Spin transport and precession experiments show the basic building blocks such as efficient spin injection, transport, detection, and dynamic functionalities. Furthermore, the magnetic properties of Fe_5GeTe_2 with multidirectional spin polarization in Fe_5GeTe_2/graphene heterostructures are revealed. The experimental results are well supported by density functional theory (DFT) calculations, where the electronic and magnetic properties of Fe_5GeTe_2/graphene heterostructures were investigated, specifically: magnetic moments, interatomic magnetic exchange interactions, and magnetic anisotropy energies. The

realization of room-temperature spin-valve operations advances the synergy between spintronics and vdW materials and is expected to boost the practical applications of vdW-magnet-based devices.

2. Results and Discussion

The motivation behind using Fe_5GeTe_2 (FGT) is its ferromagnetic order with Curie temperature (T_c) above room temperature[21,24,29] and an increased saturation magnetization with higher spin polarization[23,24] compared to Fe_3GeTe_2 with $T_c \approx 220$ K.[10,11] **Figure 1a** shows the unit cell of Fe_5GeTe_2, where each Fe species is labeled, and Fe1-Ge split sites are shown over the graphene layer (the shaded region shows the heterostructure considered for the DFT calculations). A ($\sqrt{3} \times \sqrt{3}$)$R30°$ cell of Fe_5GeTe_2 was used in the calculations, where two (one) Fe1 atoms are situated above Ge denoted as Fe1U (below denoted as Fe1D) (structure referred to as UDU configuration[30]), as confirmed by our scanning tunneling microscopy (STM) measurements (Figure 1b). The angle-resolved photoemission spectroscopy (ARPES) measurements (Figure 1c) show the Fermi surface map with bands exhibiting 6-fold symmetry of the hexagonal Brillouin zone, suggesting the good quality of the
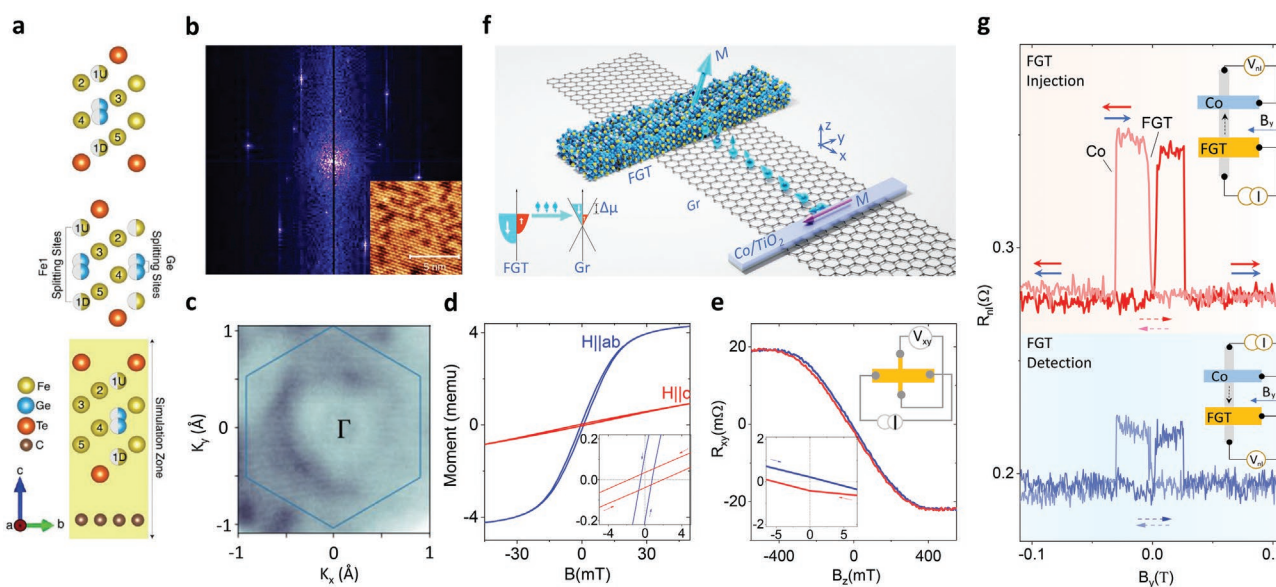

Figure 1. Room-temperature spin-valve with Fe_5GeTe_2/graphene heterostructure. a) Schematic figure of the Fe_5GeTe_2 (FGT)–graphene(Gr) heterostructure along (11$\bar{2}$0), where FGT has a rhombohedral symmetry with space group ($R\bar{3}m$). The half-filled solid balls represent an occupation probability of Ge and Fe1 atoms. The shaded area represents the interfacial part, which is modeled in DFT calculations. b) Fourier transformed image of the STM topography (inset) measured at room temperature. c) ARPES measurement of FGT at 24 K showing the electronic band structure in the k_x–k_y plane at binding energy $E_B = 0$. d) SQUID measurements of the bulk FGT crystal with in-plane and out-of-plane B field at 293 K. The inset shows the magnified hysteresis loop with finite remanence and coercive fields. e) Anomalous Hall effect (AHE) signal ($R_{xy} = V_{xy}/I$) of FGT thin flake (≈ 30 nm) with magnetic field B_z sweep along the z-axis. The schematic in the top right inset shows the AHE measurement geometry. The bottom left inset is the zoom-in of AHE data in the low B field range. The linear background has been subtracted. f) Schematic of a spin-valve device with FGT on a graphene (Gr) channel with reference Co/TiO$_2$ electrode. The bottom left inset is a schematic illustration for spin injection from FGT into the graphene channel through the vdW gap, inducing a non-equilibrium spin accumulation $\Delta \mu$ in graphene. g) The measured nonlocal (NL) spin-valve signal $R_{nl} = V_{nl}/I_{dc}$ for spin injection from FGT with parallel (P) and antiparallel (AP) alignment of FGT and Co electrodes (red and blue arrows) on CVD graphene channel with an applied bias current I across the FGT/Gr junction and NL voltage V_{nl} measured by the Co detector, as shown in the measurement geometry in the inset. The reference Au/Ti contacts on FGT and graphene are represented by the black dots. The bottom panel shows the data for FGT as the detector and Co as an injector (schematic in the inset). The red (blue) dashed arrows show the magnetic field sweep directions. The switching fields for FGT and Co electrodes in the spin-valve measurement are indicated. The measurements were performed in Dev 1 at room temperature.

crystal. The magnetic characterization of bulk Fe_5GeTe_2 crystals by the superconducting quantum interference device (SQUID) magnetometer shows a finite magnetic remanence up to room temperature in both in-plane and out-of-plane orientation, with an in-plane magnetic anisotropy (Figure 1d). However, anomalous Hall effect (AHE) measurements on thin Fe_5GeTe_2 flake ($\approx$30 nm) show a strong out-of-plane anisotropy at low temperature and a finite magnetic remanence up to room temperature (see Figure 1e; Note S1, Supporting Information).

The room-temperature vdW magnet Fe_5GeTe_2 in a heterostructure with graphene has been utilized to demonstrate spin valve devices as schematically shown in Figure 1f, where each device consisting of a Fe_5GeTe_2 flake as a spin injector or detector on the graphene spin transport channel (chemical vapor deposited CVD[31] or exfoliated graphene) (for details see Experimental Section and Figure S2, Supporting Information). The spin-valve and Hanle spin precession measurements are sensitive to the Fe_5GeTe_2/graphene interface and should allow probing of the different spin polarization components (S_x, S_y, S_z). The spin-valve measurements with the magnetic field (B_y) sweep along the y-axis can provide information about the in-plane spin polarization (S_y) along the y-axis, whereas the Hanle spin precession measurements with $B_{x(z)}$ along the $x(z)$-axis is a reliable approach to extract the (initial) spin polarization S_y and $S_{z(x)}$ and spin dynamic properties. The FGT–Co spin valve was measured using Fe_5GeTe_2 for both spin injection and detection in Dev 1 at room temperature (Figure 1g). By comparing with the reference Co–Co spin valve (Figure S3, Supporting Information), The switching (coercive) fields (H_c) for the Fe_5GeTe_2 and Co contacts can be confirmed. The observation of the robust spin-valve signals with a sharp switching

demonstrates the presence of an in-plane spin component S_y at the Fe_5GeTe_2/graphene interface at room temperature.[21,23,24] To investigate the in-plane remanence of the Fe_5GeTe_2, minor loop measurements with the same nonlocal geometry were performed, while the B_y field was swept backward before reaching the H_c of the Co electrode (Figure S3, Supporting Information).

To probe different spin polarization orientations at the Fe_5GeTe_2/graphene interface, we performed spin precession experiments in both the x-axis Hanle (xHanle) and the z-axis Hanle (zHanle) measurement geometries.[32] **Figure 2**a schematically shows the expected xHanle lineshape for different spin components (S_x, S_y, S_z) injected from Fe_5GeTe_2 with different magnetic moments (M_x, M_y, M_z). The injected out-of-plane spins S_z should result in an antisymmetric xHanle curve, whereas the spins along S_y should generate a symmetric xHanle signal. However, the spins along the S_x direction should not precess, resulting in the absence of a signal due to a collinear relationship with B_x. A sine-shaped xHanle signal is observed in the FGT–Co device (Figure 2b), indicating a possible out-of-plane spin S_z injection from the Fe_5GeTe_2/graphene interface due to the perpendicular magnetic anisotropy (PMA) of Fe_5GeTe_2 in the remanence.[33,34] The magnetic-moment-dependent xHanle signal shows a sign change with the parallel (P) and antiparallel (AP) states, also offering us a method to eliminate the non-spin precession-related background. The difference in resistance between P and AP states $R_{avg} = [R_{nl}(P) - R_{nl}(AP)]/2$ was averaged (avg) and then decomposed into symmetric (sym) and antisymmetric (asym) components with $R_{asym} = [R_{avg}(B) + R_{avg}(-B)]/2$; $R_{sym} = [R_{avg}(B) - R_{avg}(-B)]/2$, corresponding to the spin components S_y and S_z, respectively. Notably, there is no symmetric Hanle component,
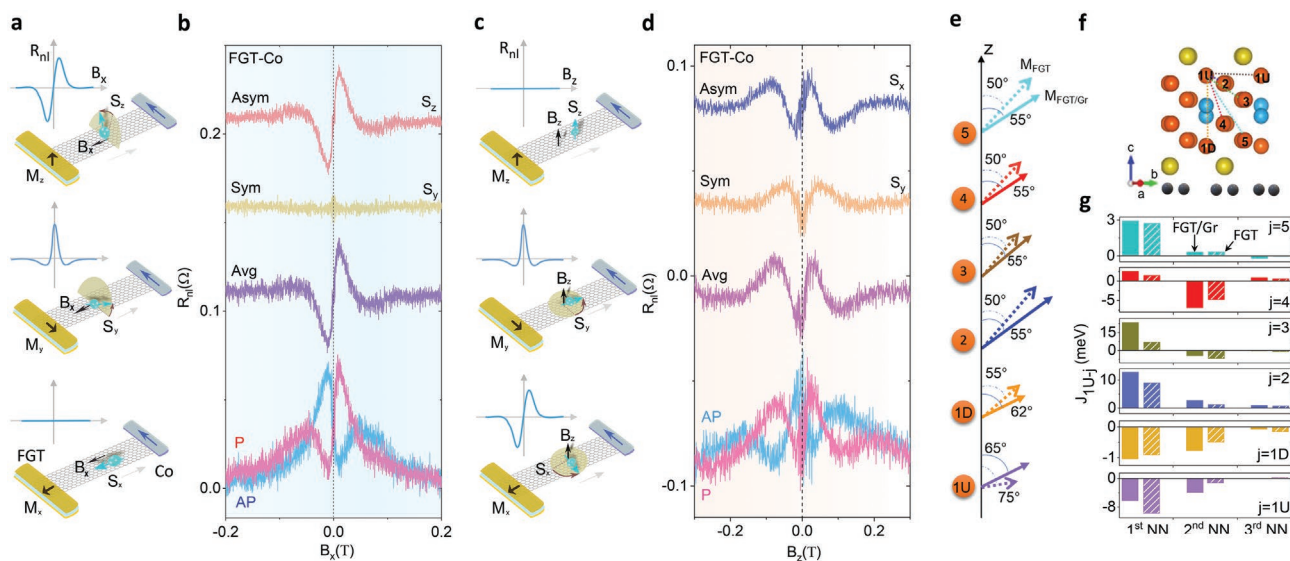

Figure 2. Hanle spin precession in Fe_5GeTe_2/graphene heterostructure at room temperature. a,c) Schematics of xHanle and zHanle measurement geometries with B_x and B_z field sweeps respectively, and the expected lineshape of the spin precession signal for all the possible FGT magnetization scenarios (M_x, M_y, and M_z). b,d) Measured xHanle and zHanle signals in the FGT–Co spin valve with different magnetic configurations (P/AP) of the electrodes. The averaged (Avg) Hanle signal and extracted symmetric (Sym) and antisymmetric (Asym) components are presented with a shift on the y-axis for clarity. e) Schematic figure showing canting of the different Fe magnetic moments in the UDU structure with respect to the z-axis in the presence (solid arrows) and absence (dashed arrows) of graphene at T = 300 K obtained from Monte Carlo simulations. f) Exchange couplings are indicated between Fe1U and Fe at other positions in the UDU structure of the FGT monolayer. g) Calculated isotropic symmetric exchange interaction parameters between the Fe1U and the nearest neighbor (NN) Fe with (solid bars) and without (dashed bars) graphene, calculated using DFT at T = 0 K.

**ADVANCED
SCIENCE NEWS**

www.advancedsciencenews.com

**ADVANCED
MATERIALS**

www.advmat.de

suggesting no remnant S_y component when a B_x is applied, which is due to a soft magnetic property of the Fe_5GeTe_2 magnetization. This is consistent with a small H_c and a narrow minor loop observed for the Fe_5GeTe_2 in the spin-valve measurements. These xHanle measurements suggest an out-of-plane magnetic anisotropy at the Fe_5GeTe_2/graphene interface with spin polarization S_z in remanence (Note S2, Supporting Information).

Similarly, the in-plane spin polarizations $S_{y(x)}$ in the FGT–Co device were evaluated based on the symmetric and antisymmetric characteristics of the measured zHanle curves (Figure 2c). In contrast, the S_z spin polarization should not result in a signal, as it is collinear with B_z. The measured zHanle signal of the FGT–Co spin-valve device (Figure 2d) suggests the injection of both spins, S_x and S_y, from the Fe_5GeTe_2/graphene interface. Measurements with the different magnetization directions of the magnetic moments (P/AP) result in the sign reversal of the Hanle curves, which are then averaged (R_{avg}) and decomposed into symmetric (Sym) and antisymmetric (Asym) components, corresponding to the spin components S_y and S_x, respectively. However, the magnitude of the S_x and S_y signals are much smaller than the measured S_z signal, confirming stronger out-of-plane magnetic moment in remanence at the Fe_5GeTe_2/graphene interface. To be noted, the presence of canted magnetism can offer such multidirectional spin polarization in Fe_5GeTe_2 (Note S3, Supporting Information).

Our DFT calculations show the magnetization for monolayer Fe_5GeTe_2 in a heterostructure with graphene to be directed along the out-of-plane or z-direction with magnetic anisotropy energy (MAE) 0.05 meV per Fe (Experimental Section and Note S4, Supporting Information). Such a weak MAE can give rise to significantly canted moments with respect to the easy axis. Figure 2e schematically shows the calculated magnitude (represented by arrow length) and the canting angle of the magnetic moment for each Fe species of Fe_5GeTe_2, with respect to the z-axis at 300 K with and without graphene, respectively (Table S3, Supporting Information). A small variation of the canting angle of Fe_5GeTe_2 is estimated from DFT calculations for with/without graphene, which changes on average by ≈3° from 55° to 58°. In the presence of graphene, the canting for Fe1U (Fe1D) decreases (increases) by 10° (7°); however, it does not have much influence on the canting angles for Fe2-5 (Note S5, Supporting Information). The canting angles averaged over all the Fe sites of the UDU structure obtained from Monte Carlo simulations is ≈58°, while from the experiments the canting angle is found to be ≈20°. There can be several possibilities that could be responsible for such discrepancy. As already mentioned, the calculations are performed using monolayer Fe_5GeTe_2, whereas in the experiments a ≈30 nm-thick flake is measured. Moreover, the calculations are performed using a pristine sample, whereas in reality, the Fe_5GeTe_2 system hosts some Fe-vacancies, and this system is a mixture of the $\sqrt{3} \times \sqrt{3}$ cells (with Fe1-Ge split-sites) and a 1×1 cell (without any split-site). Our first-principles calculations have shown that the presence of a Fe-vacancy tends to make the magnetic anisotropy more out-of-plane.[30] Regarding the experimental canting angle of Fe_5GeTe_2 with doping in graphene, we find a small variation of ≈5° by comparing differently doped graphene devices (Note S9, Supporting Information).

The moment of Fe1U increases significantly in the presence of graphene, while there is almost no influence on Fe at other positions in the UDU structure. Further, the nature and magnitude of the isotropic symmetric exchange interactions J_{1U-j} for Fe1U of Fe_5GeTe_2 were investigated with and without the graphene layer (Figure 2f,g), where the positive and negative sign of J_{1U-j} implies ferromagnetic (FM) and antiferromagnetic (AFM) interactions, respectively. In most cases, the presence of graphene increases the strength of FM interactions, while J_{1U-j} couplings tend to be more AFM-type without graphene. Such features are quite prominently visible for $j = 3$ and $j = 1U$ (Figure S9, Supporting Information). The significant increase in the moment of Fe1U in the presence of graphene is caused by the increase in bond lengths of Fe1U with its nearest neighbors-upper Te atom Te(U) and Fe2 (Table S2, Supporting Information), which in turn modifies the hybridization of Fe1U with its neighbors, enhancing the moment of Fe1U.

To figure out the anisotropic characteristic of the Fe_5GeTe_2/graphene interface, an angle-dependent in-plane spin-valve measurement was performed from +90° to −90° in the xy-plane (**Figure 3**a–c). By extracting the anti-symmetric precession and stage-like components from the in-plane results, we plot the angle dependence of the spin polarization S_z and S_y (Figure 3d,e). The measurements show that the in-plane magnetic moment of Fe_5GeTe_2 (and the corresponding spin polarization $S_{y(x)}$) can be easily rotated in the xy-plane by a small B field; however, it has a robust out-of-plane spin polarization S_z (Note S7, Supporting Information). In addition, the spin detection at the Fe_5GeTe_2/graphene interface in Dev 1 was measured (Note S8, Supporting Information) and similar results were also observed in Dev 2 with the exfoliated graphene channel (Note S9, Supporting Information).

To be noted, the SQUID, AHE, and spin-valve data can represent different magnetic properties of the Fe_5GeTe_2. The SQUID and AHE data show the magnetic property of a bulk and a thin flake, respectively, whereas the spin polarization obtained from spin-valve measurements is mainly from the contribution of the Fe_5GeTe_2/graphene interface. This is due to the weak interlayer magnetic interaction,[35,36] so that only a few layers of Fe_5GeTe_2 at the interface with graphene contribute to the spin valve signals. Moreover, the Fe_5GeTe_2/graphene interface area in different devices has a size of ≈1–3 μm², comparable to the expected Fe_5GeTe_2 magnetic domain size,[21,37] which can explain the non-zero remanence at the injection/detection areas. Moreover, our DFT results also show that the magnetic properties can be modulated at the Fe_5GeTe_2/graphene interface.

To examine the sign of the spin polarization of the Fe_5GeTe_2/graphene interface results from bias dependence measurements were compared with results obtained from the standard Co–Co spin-valve (**Figure 4**a). Reversing the bias current polarity ($+/−I$) results in the spin accumulation with opposite spin polarization in graphene due to spin injection and extraction at the Fe_5GeTe_2/graphene interface. The spin signals invert the sign for $+/−I$, and the magnitude of the spin-valve signal scales linearly with the applied bias current for Fe_5GeTe_2 and Co contacts (Figure 4b). Importantly, we notice that the sign of the spin signal for the FGT–Co spin-valve is opposite compared to that of the standard Co–Co spin-valves, which implies
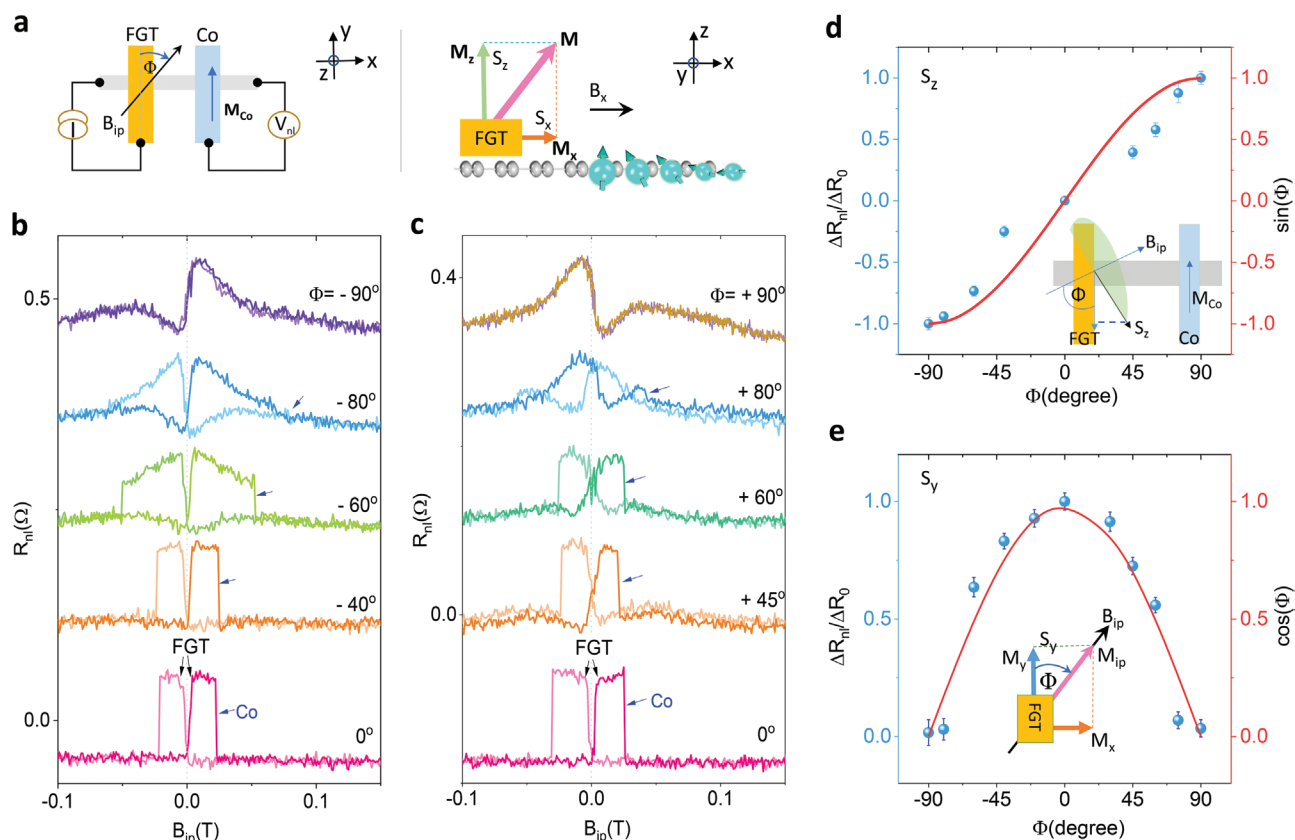
**ADVANCED
SCIENCE NEWS**

www.advancedsciencenews.com

**ADVANCED
MATERIALS**

www.advmat.de

Figure 3. Angle dependence and spin precession in Fe$_5$GeTe$_2$/graphene heterostructure at room temperature. a) The schematic top view of the spin valve device with in-plane B_{ip} field sweep in the xy-plane with an angle Φ to the y-axis. Right: Schematic front view of the device for magnetic moment configuration in FGT with an external B_x field. M is the magnetic moment with components M_x (M_z) along the $x(z)$-axis. S_x and S_z are the corresponding injected spin orientations. b,c) In-plane angle dependence of the spin valve signal with angle $\Phi = 0$ to $-90°$ and 0 to $+90°$, respectively. The switchings of injector FGT and detector Co electrodes in the spin valve signal are shown by the black and blue arrows, respectively. A linear y-axis shift is added to the signals for clarity, and a small hysteresis of ≈3.5 mT from the magnet is corrected using control experiments of reference Co–Co Hanle signals. d,e) Normalized spin-valve signal components $S_{z(y)}$ and comparison with the sine (cosine) function with the in-plane B_{ip} rotation angle Φ. The error bars were calculated from the background noise of the signal. The insets are the top view of the schematic for the in-plane magnetic moment M_{ip} projection on the axes, where $S_{z(y)}$ are injected spins from magnetic moments $M_{z(y)}$ of FGT. The measurements were performed in Dev 1 at room temperature.

negative or opposite spin polarization of the Fe$_5$GeTe$_2$/graphene interface compared to Co electrodes (Note S10, Supporting Information). Such a negative spin polarization is found to be robust and could be reproducibly observed in all devices (Figures S17 and S20 in Supporting Information for Dev 2 and 3). These observations agree with the density of states (DOS) obtained from DFT calculations (Figure 4d), where Fe$_5$GeTe$_2$ shows a negative spin polarization at the Fermi energy (E_F) with the DOS of the minority channel being larger than that of the majority channel at the Fe$_5$GeTe$_2$/graphene interface. To have a better insight, the sublattice-resolved spin polarization at E_F is given in Table S5 (Supporting Information), where all Fe moments have negative spin polarization, and Ge and Te have positive spin polarization.

Considering the different resistances of Fe$_5$GeTe$_2$/graphene interfaces and the geometrical parameters of the devices, a calculation of the spin-signal versus interface resistance based on the drift-diffusion model[47] was performed. The spin transport in graphene is not affected by spin absorption effects in Dev 1 and Dev 2, which have a large Fe$_5$GeTe$_2$/graphene

interface resistance with a minimum conductance mismatch (Figure 4e). The spin diffusion length and interface resistances for both CVD and exfoliated graphene are similar. Noticeably, the difference in square resistance R_{sq} between CVD graphene (1–5 kΩ) and exfoliated few-layer graphene (0.2–0.5 kΩ) makes the calculated curves different (Note S15, Supporting Information).

Finally, the spin polarization of the Fe$_5$GeTe$_2$/graphene interface was calculated by considering both the spin valve and the Hanle signals. The magnitude of the spin-valve signal can be defined as $\Delta R_{nl} = P_{ip}P_{Co}\lambda_{gr}R_{sq}\exp(-L_{ch}/\lambda_{gr})/w_{gr}$, where only the in-plane spin polarization of Fe$_5$GeTe$_2$, P_{ip}, is unknown; and the other parameters are extracted from the Co–Co reference zHanle measurements[32] (P_{Co} is the spin polarization of Co contacts, λ_{gr} the spin diffusion length, R_{sq} the square resistance, L_{ch} the channel length and w_{gr} the width of the graphene channel). The calculated in-plane spin polarizations for the different devices cover the range $|P_{ip}| = 1.2$–44.9%. The calculated out-of-plane spin polarization was extracted to be $|P_z| = 3$–9.5% from the xHanle data. It should be noted that the
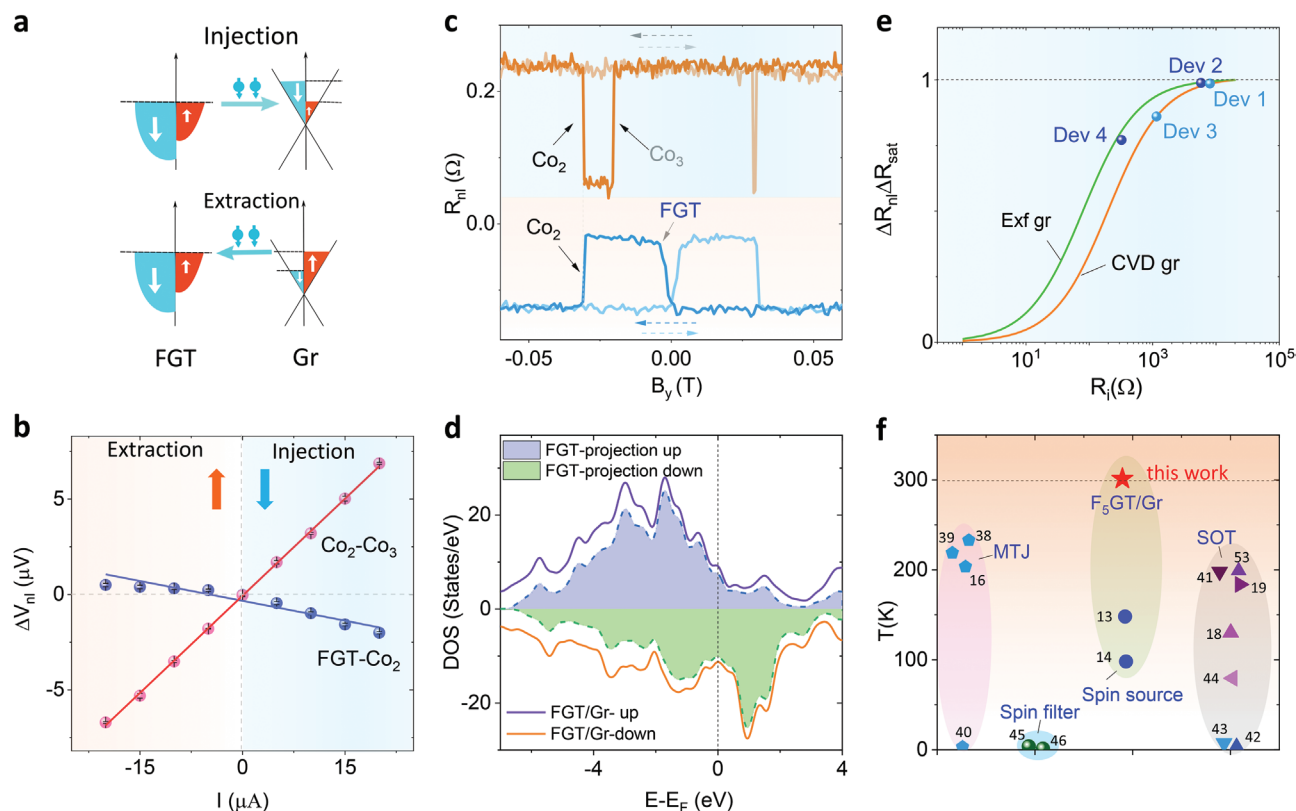
Figure 4. Negative spin polarization of Fe_5GeTe_2/graphene interface. a) Schematics for the spin injection and extraction process at FGT/Gr interface, showing the accumulation of "down" and "up" spins in the graphene channel, respectively. b) Bias dependence of the FGT–Co_2 and Co_2–Co_3 spin-valve signal magnitude in the spin injection and extraction regime and the linear fittings, respectively. $Co_{2(3)}$ are the reference Co electrodes. The error bars are calculated from the standard deviation of the measured data. c) Comparison of the measured spin valve signals of FGT–Co_2 and Co_2–Co_3 spin devices. The signals are shifted along the y-axis for clarity. d) Calculated spin-polarized total DOS for Fe_5GeTe_2/graphene heterostructure (solid lines) and projected onto Fe_5GeTe_2 (color-shaded area). e) The calculated spin valve signal magnitude (normalized) as a function of the interface resistance (R_i) for CVD graphene and exfoliated (Exf) graphene samples. All the parameters were taken from the measured FGT devices. f) Comparison of the working temperature of our FGT–graphene spin-valve devices with the state-of-art results on vdW-magnet-based devices, like MTJs: Fe_3GeTe_2/hBN,[16] Fe_3GeTe_2/MoS_2,[38] Fe_3GeTe_2/InSe,[39] Fe_3GeTe_2/WSe_2;[40] spin source devices: CrSBr/gr,[14] $Cr_2Ge_2Te_6$/gr;[13] SOT devices: Fe_3GeTe_2/Pt,[18,19] Fe_3GeTe_2/WTe_2,[41,53] $Cr_2Ge_2Te_6$/$(Bi_{1-x}Sb_x)_2Te_3$,[42] $Cr_2Ge_2Te_6$/Pt,[43] $Cr_2Ge_2Te_6$/Ta,[44] and spin filter devices: CrI_3/CrI_3.[45,46]

saturated in-plane spin polarization is different from the out-of-plane remanence spin polarization in Fe_5GeTe_2. Detailed spin parameters of the different devices are summarized in Table S4 (Supporting Information). The observed variation of the spin polarization in different devices can be due to compositional variations between different Fe_5GeTe_2 flakes[37] as well as different Fe_5GeTe_2/graphene interface conditions.[48,49] The DFT calculations show a negative spin polarization of the Fe_5GeTe_2/graphene interface with $p \approx -10\%$ (Table S5, Supporting Information). As suggested by the DFT calculations, the oxidation of Fe_5GeTe_2 at the interface can be one explanation for the large spin polarization observed in the exfoliated-graphene device prepared in air, in contrast to CVD-graphene devices prepared in a glovebox (Note S16, Supporting Information). However, changing the vdW gap by 5% does not have a significant impact on the spin polarization and magnetic moments (Note S17, Supporting Information). The observation of robust room temperature spin valve and Hanle signals suggests efficient spin injection/detection for the Fe_5GeTe_2/graphene vdW heterostructures and provides a substantial advance in vdW-magnet-based device applications (Figure 4f).

3. Summary and Outlook

We have demonstrated room temperature operation of vdW-magnet-based lateral spin-valve devices using Fe_5GeTe_2/graphene vdW heterostructures. Highly efficient spin injection, transport, and detection could be observed with a negative spin polarization at the Fe_5GeTe_2/graphene interfaces. These spin-valve devices allowed us to probe different spin-polarization components and their relationship with spin transport and precession in the device. The observed multidirectional spin polarization at the Fe_5GeTe_2/graphene interface indicates an out-of-plane canted magnetism. The strong remanent magnetization in the Fe_5GeTe_2/graphene heterostructure is different from the bulk behavior of Fe_5GeTe_2 and can be ascribed to the van der Waals heterostructure interface. The canted magnetization and negative spin polarization are supported by DFT calculations and Monte Carlo simulations of the Fe_5GeTe_2/graphene system. The possibility to integrate vdW magnets with graphene spin valve devices has enormous potential in developing vdW heterostructure-based spintronics at room temperature.[28,49,50] The canted and soft magnetic properties of Fe_5GeTe_2 at room

temperature can be useful for field-free spin-orbit torque-based technologies.[51] This will bring a strong synergy between 2D materials and spintronics with the possibility of further controlling the figures of merit by twist angle between the vdW layers, magnetic proximity effects, and gate tunability for energy-efficient and ultrafast spintronic devices.[15,52] These room-temperature developments in vdW-magnet-based heterostructures will open future opportunities for fundamental studies and spintronic devices for magnetic sensors, memory, logic, communication, and novel computing architecture applications.[25,26]

4. Experimental Section

Fabrication of Spin-Valve Devices and Spin Transport Measurements: The Fe_5GeTe_2 crystals were obtained from Hq Graphene, the large area CVD graphene samples were received from Grolltex Inc on a 4-inch SiO_2/Si wafer, and HOPG graphite was used to obtain few-layer exfoliated graphene samples. The CVD graphene channels were first prepared by electron beam lithography (EBL) and oxygen plasma etching process. The Fe_5GeTe_2 flakes (≈ 20–50 nm) were exfoliated and dry transferred onto both monolayer CVD graphene and exfoliated few-layer graphene on an $n^{++}Si$ substrate with 285 nm SiO_2. The exfoliation of Fe_5GeTe_2 and their heterostructures with CVD graphene were prepared inside a glove box in an N_2 atmosphere, where a clean interface can be obtained (Dev 1 and Dev 3). The Dev 2 and Dev 4 with Fe_5GeTe_2/exfoliated graphene heterostructures were prepared in air (inside the cleanroom environment), followed by a vacuum process in a high vacuum chamber. For the device fabrication, the nonmagnetic and magnetic contacts were prepared by multiple electron beam lithography (EBL) processes and electron beam evaporation of metals. The nonmagnetic Au/Ti contacts were first prepared on Fe_5GeTe_2 flakes with 10 s low-energy Ar cleaning of the surface at a glancing angle. Next, the nonmagnetic Au/Ti contacts were prepared on graphene for reference electrodes by EBL and lift-off process. The ferromagnetic contacts (Co/TiO$_2$) on graphene were prepared by EBL and electron beam evaporation and lift-off process. For the Co/TiO$_2$ contacts, a two-step deposition and an oxidation process were adopted; 0.4 nm Ti was deposited, followed by a 10 Torr O_2 oxidation for 10 min each, followed by 60 nm of Co deposition. Measurements were performed at room temperature with a magnetic field up to 0.6 Tesla and a sample rotation stage in vacuum conditions. The measurement system was calibrated with standard all CoCo graphene spin-valve measurements. The electronic measurements were carried out using the current source Keithley 6221, nanometer 2182A, and dual-channel source meter Keithley 2612B. All the spin valve and Hanle measurements were performed at room temperature.

Characterization of Fe_5GeTe_2: The angle-resolved photoelectron spectroscopy (ARPES) measurements were performed at the MAX IV Laboratory Bloch beamline with high energy, angular, and spatial resolution (15 meV, <0.15 degrees, 10 μmx15 μm). The measurements were done at 24 K at 145 eV photon energy. Single crystals of Fe_5GeTe_2 were cleaved in a high vacuum better than 8×10^{-11} mbar. A deflector-type hemispherical analyzer from Scienta-Omicron was used. The scanning tunneling microscopy (STM) measurements were done at 300 K using the VT-XA model from Scienta-Omicron. Chemically etched W tips were used and further cleaned by e-beam heating. A superconducting quantum interference device (SQUID) was used to measure the static magnetic properties of bulk Fe_5GeTe_2 crystals at room temperature (293 K). Isothermal magnetization measurements were performed with the magnetic field applied both in-plane ($B\|xy$) and out-of-plane ($B\|z$). The bulk Fe_5GeTe_2 crystal was glued on a Si substrate to achieve proper alignment of the magnetic field during the measurements.

DFT Calculations: Density functional theory (DFT) calculations were performed using the Vienna Ab Initio Simulation Package (VASP), where the generalized gradient approximation (GGA) was used as the exchange-correlation functional. The interatomic isotropic symmetric exchange parameters J_{ij} of the Heisenberg model were calculated using the full-potential linear muffin-tin orbital method (FP-LMTO) and the relativistic spin-polarized toolkit (RSPt). Monte Carlo simulations using the parametrized Heisenberg model with isotropic and anisotropic terms were performed by UppASD code to calculate canting angles. Details of the computations are provided in the Supporting Information.

Supporting Information

Supporting Information is available from the Wiley Online Library or from the author.

Author Contributions

B.Z. and R.N. fabricated and characterized the devices. R.G. and P.S. performed SQUID measurements, S.G, S.E., and B.S. performed theoretical calculations and analysis, K.A., C.P., B.S. performed STM and ARPES measurements, A.M.H., B.K., D.K., A.K. supported in device preparation and measurements. S.P.D. conceived the idea and supervised the experimental research. All authors participated in the interpretation of data, compiled the figures, and wrote the manuscript.

Conflict of Interest

The authors declare no conflict of interest.

Data Availability Statement

The data that support the findings of this study are available from the corresponding author upon reasonable request.

[1] A. K. Geim, I. V. Grigorieva, *Nature* **2013**, *499*, 419.

[2] K. S. Novoselov, A. Mishchenko, A. Carvalho, A. H. Castro Neto, *Science* **2016**, *353*, aac9439.

[3] I. Žutić, A. Matos-Abiague, B. Scharf, H. Dery, K. Belashchenko, *Mater. Today* **2019**, *22*, 85.

[4] M. Gibertini, M. Koperski, A. F. Morpurgo, K. S. Novoselov, *Nat. Nanotechnol.* **2019**, *14*, 408.

[5] C. Gong, X. Zhang, *Science* **2019**, *363*, eaav4450.

[6] S. Lebègue, T. Björkman, M. Klintenberg, R. M. Nieminen, O. Eriksson, *Phys. Rev. X* **2013**, *3*, 031002.

[7] C. Gong, L. Li, Z. Li, H. Ji, A. Stern, Y. Xia, T. Cao, W. Bao, C. Wang, Y. Wang, Z. Q. Qiu, R. J. Cava, S. G. Louie, J. X. X. Zhan, *Nature* **2017**, *546*, 265.

[8] B. Huang, G. Clark, E. Navarro-Moratalla, D. R. Klein, R. Cheng, K. L. Seyler, D. Zhong, E. Schmidgall, M. A. McGuire, D. H. Cobden, W. Yao, D. Xiao, P. Jarillo-Herrero, X. Xu, *Nature* **2017**, *546*, 270.

[9] M. Kim, P. Kumaravadivel, J. Birkbeck, W. Kuang, S. G. Xu, D. G. Hopkinson, J. Knolle, P. A. Mcclarty, A. I. Berdyugin, M. Ben Shalom, R. V. Gorbachev, S. J. Haigh, S. Liu, J. H. Edgar, K. S. Novoselov, I. V. Grigorieva, A. K. Geim, *Nat. Electron.* **2019**, *2*, 457.

[10] Z. Fei, B. Huang, P. Malinowski, W. Wang, T. Song, J. Sanchez, W. Yao, D. Xiao, X. Zhu, A. F. May, W. Wu, D. H. Cobden, J.-H. Chu, X. Xu, *Nat. Mater.* **2018**, *17*, 778.

[11] Y. Deng, Y. Yu, Y. Song, J. Zhang, N. Z. Wang, Z. Sun, Y. Yi, Y. Z. Wu, S. Wu, J. Zhu, J. Wang, X. H. Chen, Y. Zhang, *Nature* **2018**, *563*, 94.

[12] D. R. Klein, D. Macneill, J. L. Lado, D. Soriano, E. Navarro-Moratalla, K. Watanabe, T. Taniguchi, S. Manni, P. Canfield, J. Fernández-Rossier, P. Jarillo-Herrero, *Science* **2018**, *360*, 1218.

[13] B. Karpiak, A. W. Cummings, K. Zollner, M. Vila, D. Khokhriakov, A. M. Hoque, A. D. P. Svedlindh, J. Fabian, S. Roche, S. P. Dash, *2D Mater.* **2019**, *7*, 015026.

[14] T. S. Ghiasi, A. A. Kaverzin, A. H. Dismukes, D. K. De Wal, X. Roy, B. J. Van Wees, *Nat. Nanotechnol.* **2021**, *16*, 788.

[15] K. Zollner, M. Gmitra, J. Fabian, *Phys. Rev. Lett.* **2020**, *125*, 196402.

[16] Z. Wang, D. Sapkota, T. Taniguchi, K. Watanabe, D. Mandrus, A. F. Morpurgo, *Nano Lett.* **2018**, *18*, 4303.

[17] H. Zhang, D. Raftrey, Y.-T. Chan, Y.-T. Shao, R. Chen, X. Chen, X. Huang, J. T. Reichanadter, K. Dong, S. Susarla, L. Caretta, Z. Chen, J. Yao, P. Fischer, J. B. Neaton, W. Wu, D. A. Muller, R. J. Birgeneau, R. Ramesh, *Sci. Adv.* **2022**, *8*, eabm7103.

[18] X. Wang, J. Tang, X. Xia, C. He, J. Zhang, Y. Liu, C. Wan, C. Fang, C. Guo, W. Yang, Y. Guang, X. Zhang, H. Xu, J. Wei, M. Liao, X. Lu, J. Feng, X. Li, Y. Peng, H. Wei, R. Yang, D. Shi, X. Zhang, Z. Han, Z. Zhang, G. Zhang, G. Yu, X. Han, *Sci. Adv.* **2019**, *5*, eaaw8904.

[19] M. Alghamdi, M. Lohmann, J. Li, P. R. Jothi, Q. Shao, M. Aldosary, T. Su, B. P. T. Fokwa, J. Shi, *Nano Lett.* **2019**, *19*, 4400.

[20] Q. Li, M. Yang, C. Gong, R. V. Chopdekar, A. T. N'diaye, J. Turner, G. Chen, A. Scholl, P. Shafer, E. Arenholz, A. K. Schmid, S. Wang, K. Liu, N. Gao, A. S. Admasu, S.-W. Cheong, C. Hwang, J. Li, F. Wang, X. Zhang, Z. Qiu, *Nano Lett.* **2018**, *18*, 5974.

[21] H. Zhang, R. Chen, K. Zhai, X. Chen, L. Caretta, X. Huang, R. V. Chopdekar, J. Cao, J. Sun, J. Yao, R. Birgeneau, R. Ramesh, *Phys. Rev. B* **2020**, *102*, 064417.

[22] H. Wang, Y. Liu, P. Wu, W. Hou, Y. Jiang, X. Li, C. Pandey, D. Chen, Q. Yang, H. Wang, D. Wei, N. Lei, W. Kang, L. Wen, T. Nie, W. Zhao, K. L. Wang, *ACS Nano* **2020**, *14*, 10045.

[23] J. Seo, D. Y. Kim, E. S. An, K. Kim, G.-Y. Kim, S.-Y. Hwang, D. W. Kim, B. G. Jang, H. Kim, G. Eom, S. Y. Seo, R. Stania, M. Muntwiler, J. Lee, K. Watanabe, T. Taniguchi, Y. J. Jo, J. Lee, B. I. Min, M. H. Jo, H. W. Yeom, S.-Y. Choi, J. H. Shim, J. S. Kim, *Sci. Adv.* **2020**, *6*, eaay8912.

[24] A. F. May, D. Ovchinnikov, Q. Zheng, R. Hermann, S. Calder, B. Huang, Z. Fei, Y. Liu, X. Xu, M. A. Mcguire, *ACS Nano* **2019**, *13*, 4436.

[25] B. Behin-Aein, D. Datta, S. Salahuddin, S. Datta, *Nat. Nanotechnol.* **2010**, *5*, 266.

[26] S. Manipatruni, D. E. Nikonov, C.-C. Lin, T. A. Gosavi, H. Liu, B. Prasad, Y.-L. Huang, E. Bonturim, R. Ramesh, I. A. Young, *Nature* **2019**, *565*, 35.

[27] J. Grollier, D. Querlioz, K. Y. Camsari, K. Everschor-Sitte, S. Fukami, M. D. Stiles, *Nat. Electron.* **2020**, *3*, 360.

[28] D. Khokhriakov, S. Sayed, A. Md. Hoque, B. Karpiak, B. Zhao, S. Datta, S. P. Dash, *Phys. Rev. Appl.* **2022**, *18*, 064063.

[29] C. Tian, F. Pan, S. Xu, K. Ai, T. Xia, P. Chenga, *Appl. Phys. Lett.* **2020**, *116*, 202402.

[30] S. Ershadrad, S. Ghosh, D. Wang, Y. Kvashnin, B. Sanyal, *J. Phys. Chem. Lett.* **2022**, *13*, 4877.

[31] S. Roche, J. Åkerman, B. Beschoten, J.-C. Charlier, M. Chshiev, S. Prasad Dash, B. Dlubak, J. Fabian, A. Fert, M. Guimarães, F. Guinea, I. Grigorieva, C. Schönenberger, P. Seneor, C. Stampfer, S. O. Valenzuela, X. Waintal, B. Van Wees, *2D Mater.* **2015**, *2*, 030202.

[32] N. Tombros, C. Jozsa, M. Popinciuc, H. T. Jonkman, B. J. Van Wees, *Nature* **2007**, *448*, 571.

[33] C. K. Safeer, J. Ingla-Aynés, F. Herling, J. H. Garcia, M. Vila, N. Ontoso, M. R. Calvo, S. Roche, L. E. Hueso, F. Casanova, *Nano Lett.* **2019**, *19*, 1074.

[34] L. A. Benítez, W. Savero Torres, J. F. Sierra, M. Timmermans, J. H. Garcia, S. Roche, M. V. Costache, S. O. Valenzuela, *Nat. Mater.* **2020**, *19*, 170.

[35] C. Tan, W.-Q. Xie, G. Zheng, N. Aloufi, S. Albarakati, M. Algarni, J. Li, J. Partridge, D. Culcer, X. Wang, J. B. Yi, M. Tian, Y. Xiong, Y.-J. Zhao, L. Wang, *Nano Lett.* **2021**, *21*, 5599.

[36] Z. Li, W. Xia, H. Su, Z. Yu, Y. Fu, L. Chen, X. Wang, N. Yu, Z. Zou, Y. Guo, *Sci. Rep.* **2020**, *10*, 15345.

[37] T. T. Ly, J. Park, K. Kim, H.-B. Ahn, N. J. Lee, K. Kim, T.-E. Park, G. Duvjir, N. H. Lam, K. Jang, C.-Y. You, Y. Jo, S. K. Kim, C. Lee, S. Kim, J. Kim, *Adv. Funct. Mater.* **2021**, *31*, 2009758.

[38] H. Lin, F. Yan, C. Hu, Q. Lv, W. Zhu, Z. Wang, Z. Wei, K. Chang, K. Wang, *ACS Appl. Mater. Interfaces* **2020**, *12*, 43921.

[39] W. Zhu, H. Lin, F. Yan, C. Hu, Z. Wang, L. Zhao, Y. Deng, Z. R. Kudrynskyi, T. Zhou, Z. D. Kovalyuk, Y. Zheng, A. Patanè, I. Zutic, S. Li, H. Zheng, K. Wang, *Adv. Mater.* **2021**, *33*, 2104658.

[40] K.-H. Min, D. H. Lee, S.-J. Choi, I.-H. Lee, J. Seo, D. W. Kim, K.-T. Ko, K. Watanabe, T. Taniguchi, D. H. Ha, C. Kim, J. H. Shim, J. Eom, J. S. Kim, S. Jung, *Nat. Mater.* **2022**, *21*, 1144.

[41] I. Shin, W. J. Cho, E.-S. An, S. Park, H.-W. Jeong, S. Jang, W. J. Baek, S. Y. Park, D.-H. Yang, J. H. Seo, G.-Y. Kim, M. N. Ali, S.-Y. Choi, H.-W. Lee, J. S. Kim, S. D. Kim, G.-H. Lee, *Adv. Mater.* **2022**, *34*, 2101730.

[42] M. Mogi, K. Yasuda, R. Fujimura, R. Yoshimi, N. Ogawa, A. Tsukazaki, M. Kawamura, K. S. Takahashi, M. Kawasaki, Y. Tokura, *Nat. Commun.* **2021**, *12*, 1404.

[43] V. Gupta, T. M. Cham, G. M. Stiehl, A. Bose, J. A. Mittelstaedt, K. Kang, S. Jiang, K. F. Mak, J. Shan, R. A. Buhrman, D. C. Ralph, *Nano Lett.* **2020**, *20*, 7482.

[44] V. Ostwal, T. Shen, J. Appenzeller, *Adv. Mater.* **2020**, *32*, 1906021.

[45] S. Jiang, J. Shan, K. F. Mak, *Nat. Mater.* **2018**, *17*, 406.

[46] T. Song, X. Cai, M. W.-Y. Tu, X. Zhang, B. Huang, N. P. Wilson, K. L. Seyler, L. Zhu, T. Taniguchi, K. Watanabe, M. A. Mcguire, D. H. Cobden, D. Xiao, W. Yao, X. Xu, *Science* **2018**, *360*, 1214.

[47] S. Takahashi, S. Maekawa, *Phys. Rev. B* **2003**, *67*, 052409.

[48] M. Arai, R. Moriya, N. Yabuki, S. Masubuchi, K. Ueno, T. Machida, *Appl. Phys. Lett.* **2015**, *107*, 103107.

[49] J. F. Sierra, J. Fabian, R. K. Kawakami, S. Roche, S. O. Valenzuela, *Nat. Nanotechnol.* **2021**, *16*, 856.

[50] A. Avsar, H. Ochoa, F. Guinea, B. Özyilmaz, B. J. Van Wees, I. J. Vera-Marun, *Rev. Mod. Phys.* **2020**, *92*, 021003.

**ADVANCED
SCIENCE NEWS**

www.advancedsciencenews.com

**ADVANCED
MATERIALS**

www.advmat.de

[51] L. Liu, Q. Qin, W. Lin, C. Li, Q. Xie, S. He, X. Shu, C. Zhou, Z. Lim, J. Yu, W. Lu, M. Li, X. Yan, S. J. Pennycook, J. Chen, *Nat. Nanotechnol.* **2019**, *14*, 939.

[52] K. Zollner, J. Fabian, *Phys. Rev. Lett.* **2022**, *128*, 106401.

[53] I.-H. Kao, R. Muzzio, H. Zhang, M. Zhu, J. Gobbo, S. Yuan, D. Weber, R. Rao, J. Li, J. H. Edgar, J. E. Goldberger, J. Yan, D. G. Mandrus, J. Hwang, R. Cheng, J. Katoch, S. Singh, *Nat. Mater.* **2022**, *21*, 1029.

2209113 (9 of 9)